

Background-free deep imaging by spatial overlap modulation nonlinear optical microscopy

Keisuke Isobe,^{1,*} Hiroyuki Kawano,² Takanori Takeda,^{1,3} Akira Suda,³ Akiko Kumagai,² Hideaki Mizuno,² Atsushi Miyawaki,² and Katsumi Midorikawa¹

¹Laser Technology Laboratory, RIKEN Advanced Science Institute, 2-1 Hirosawa, Wako, Saitama 351-0198, Japan

²Laboratory for Cell Function Dynamics, RIKEN Brain Science Institute, 2-1 Hirosawa, Wako, Saitama 351-0198, Japan

³Department of Physics, Graduate School of Science and Technology, Tokyo University of Science, 2641 Yamazaki, Noda, Chiba 278-8510, Japan

*kisobe@riken.jp

Abstract: We demonstrate how the resolution and imaging depth limitations of nonlinear optical microscopy can be overcome by modulating the spatial overlap between two-color pulses. We suppress out-of-focus signals, which limit the imaging depth, by a factor of 100, and enhance the lateral and axial resolution by factors of 1.6 and 1.4–1.8 respectively. Using spatial overlap modulation, we demonstrate background-free three-dimensional imaging of fixed mouse brain tissue at depths for which the signals of the conventional technique are swamped by background noise from out-of-focus regions.

© 2012 Optical Society of America

OCIS codes: (180.4315) Nonlinear microscopy; (180.2520) Fluorescence microscopy; (170.5660) Raman spectroscopy; (190.4180) Multiphoton processes.

References and links

1. W. Denk, J. H. Strickler, and W. W. Webb, "Two-photon laser scanning fluorescence microscopy," *Science* **248**(4951), 73–76 (1990).
2. K. König, "Multiphoton microscopy in life sciences," *J. Microsc.* **200**(2), 83–104 (2000).
3. W. R. Zipfel, R. M. Williams, and W. W. Webb, "Nonlinear magic: multiphoton microscopy in the biosciences," *Nat. Biotechnol.* **21**(11), 1369–1377 (2003).
4. P. J. Campagnola and L. M. Loew, "Second-harmonic imaging microscopy for visualizing biomolecular arrays in cells, tissues and organisms," *Nat. Biotechnol.* **21**(11), 1356–1360 (2003).
5. F. Légaré, C. Pfeffer, and B. R. Olsen, "The role of backscattering in SHG tissue imaging," *Biophys. J.* **93**(4), 1312–1320 (2007).
6. J. Squier and M. Müller, "High resolution nonlinear microscopy: A review of sources and methods for achieving optimal imaging," *Rev. Sci. Instrum.* **72**(7), 2855–2867 (2001).
7. Y. Barad, H. Eisenberg, M. Horowitz, and Y. Silberberg, "Nonlinear scanning laser microscopy by third harmonic generation," *Appl. Phys. Lett.* **70**(8), 922–924 (1997).
8. M. D. Duncan, J. Reintjes, and T. J. Manuccia, "Scanning coherent anti-Stokes Raman microscope," *Opt. Lett.* **7**(8), 350–352 (1982).
9. A. Zumbusch, G. R. Holtom, and X. S. Xie, "Three-dimensional vibrational imaging by coherent anti-Stokes Raman scattering," *Phys. Rev. Lett.* **82**(20), 4142–4145 (1999).
10. K. Isobe, S. Kataoka, R. Murase, W. Watanabe, T. Higashi, S. Kawakami, S. Matsunaga, K. Fukui, and K. Itoh, "Stimulated parametric emission microscopy," *Opt. Express* **14**(2), 786–793 (2006).
11. K. Isobe, T. Kawasumi, T. Tamaki, S. Kataoka, Y. Ozeki, and K. Itoh, "Three-dimensional profiling of refractive index distribution inside transparent materials by use of nonresonant four-wave mixing microscopy," *Appl. Phys. Express* **1**, 022006 (2008).
12. W. S. Warren, M. C. Fischer, and T. Ye, "Novel nonlinear contrast improves deep-tissue microscopy," *Laser Focus World* **43**, 99–103 (June 1, 2007).
13. C. W. Freudiger, W. Min, B. G. Saar, S. Lu, G. R. Holtom, C. He, J. C. Tsai, J. X. Kang, and X. S. Xie, "Label-free biomedical imaging with high sensitivity by stimulated Raman scattering microscopy," *Science* **322**(5909), 1857–1861 (2008).
14. P. Nandakumar, A. Kovalev, and A. Volkmer, "Vibrational imaging based on stimulated Raman scattering microscopy," *New J. Phys.* **11**(3), 033026 (2009).
15. Y. Ozeki, F. Dake, S. Kajiyama, K. Fukui, and K. Itoh, "Analysis and experimental assessment of the sensitivity of stimulated Raman scattering microscopy," *Opt. Express* **17**(5), 3651–3658 (2009).
16. P. Tian and W. S. Warren, "Ultrafast measurement of two-photon absorption by loss modulation," *Opt. Lett.* **27**(18), 1634–1636 (2002).

17. P. Theer, M. T. Hasan, and W. Denk, "Two-photon imaging to a depth of 1000 μm in living brains by use of a $\text{Ti}:\text{Al}_2\text{O}_3$ regenerative amplifier," *Opt. Lett.* **28**(12), 1022–1024 (2003).
18. D. Kobat, M. E. Durst, N. Nishimura, A. W. Wong, C. B. Schaffer, and C. Xu, "Deep tissue multiphoton microscopy using longer wavelength excitation," *Opt. Express* **17**(16), 13354–13364 (2009).
19. P. Theer and W. Denk, "On the fundamental imaging-depth limit in two-photon microscopy," *J. Opt. Soc. Am. A* **23**(12), 3139–3149 (2006).
20. G. Zhu, J. van Howe, M. Durst, W. Zipfel, and C. Xu, "Simultaneous spatial and temporal focusing of femtosecond pulses," *Opt. Express* **13**(6), 2153–2159 (2005).
21. D. Oron, E. Tal, and Y. Silberberg, "Scanningless depth-resolved microscopy," *Opt. Express* **13**(5), 1468–1476 (2005).
22. A. Leray and J. Mertz, "Rejection of two-photon fluorescence background in thick tissue by differential aberration imaging," *Opt. Express* **14**(22), 10565–10573 (2006).
23. N. Ji, D. E. Milkie, and E. Betzig, "Adaptive optics via pupil segmentation for high-resolution imaging in biological tissues," *Nat. Methods* **7**(2), 141–147 (2010).
24. M. A. A. Neil, R. Juskaitis, and T. Wilson, "Method of obtaining optical sectioning by using structured light in a conventional microscope," *Opt. Lett.* **22**(24), 1905–1907 (1997).
25. N. Chen, C.-H. Wong, and C. J. R. Sheppard, "Focal modulation microscopy," *Opt. Express* **16**(23), 18764–18769 (2008).
26. S. W. Hell and J. Wichmann, "Breaking the diffraction resolution limit by stimulated emission: stimulated-emission-depletion fluorescence microscopy," *Opt. Lett.* **19**(11), 780–782 (1994).
27. E. Betzig, G. H. Patterson, R. Sougrat, O. W. Lindwasser, S. Olenych, J. S. Bonifacino, M. W. Davidson, J. Lippincott-Schwartz, and H. F. Hess, "Imaging intracellular fluorescent proteins at nanometer resolution," *Science* **313**(5793), 1642–1645 (2006).
28. S. T. Hess, T. P. K. Girirajan, and M. D. Mason, "Ultra-high resolution imaging by fluorescence photoactivation localization microscopy," *Biophys. J.* **91**(11), 4258–4272 (2006).
29. M. J. Rust, M. Bates, and X. Zhuang, "Sub-diffraction-limit imaging by stochastic optical reconstruction microscopy (STORM)," *Nat. Methods* **3**(10), 793–796 (2006).
30. K. Fujita, M. Kobayashi, S. Kawano, M. Yamanaka, and S. Kawata, "High-resolution confocal microscopy by saturated excitation of fluorescence," *Phys. Rev. Lett.* **99**(22), 228105 (2007).
31. K. Isobe, A. Suda, H. Hashimoto, F. Kannari, H. Kawano, H. Mizuno, A. Miyawaki, and K. Midorikawa, "High-resolution fluorescence microscopy based on a cyclic sequential multiphoton process," *Biomed. Opt. Express* **1**(3), 791–797 (2010).
32. M. G. L. Gustafsson, "Surpassing the lateral resolution limit by a factor of two using structured illumination microscopy," *J. Microsc.* **198**(2), 82–87 (2000).
33. G. Moneron and S. W. Hell, "Two-photon excitation STED microscopy," *Opt. Express* **17**(17), 14567–14573 (2009).
34. P. E. Hänninen, S. W. Hell, J. Salo, E. Soini, and C. Cremer, "Two-photon excitation 4Pi confocal microscope: Enhanced axial resolution microscope for biological research," *Appl. Phys. Lett.* **66**(13), 1698–1700 (1995).
35. M. R. Beversluis and S. J. Stranick, "Enhanced contrast coherent anti-Stokes Raman scattering microscopy using annular phase masks," *Appl. Phys. Lett.* **93**(23), 231115 (2008).
36. R. Boyd, *Nonlinear Optics*, 3rd ed. (Academic, 2008).
37. G. Feng, R. H. Mellor, M. Bernstein, C. Keller-Peck, Q. T. Nguyen, M. Wallace, J. M. Nerbonne, J. W. Lichtman, and J. R. Sanes, "Imaging neuronal subsets in transgenic mice expressing multiple spectral variants of GFP," *Neuron* **28**(1), 41–51 (2000).
38. K. Isobe, A. Suda, M. Tanaka, H. Hashimoto, F. Kannari, H. Kawano, H. Mizuno, A. Miyawaki, and K. Midorikawa, "Nonlinear optical microscopy and spectroscopy employing octave spanning pulses," *IEEE J. Sel. Top. Quantum Electron.* **16**(4), 767–780 (2010).
39. N. T. Urban, K. I. Willig, S. W. Hell, and U. V. Nägerl, "STED nanoscopy of actin dynamics in synapses deep inside living brain slices," *Biophys. J.* **101**(5), 1277–1284 (2011).
40. S. Lu, W. Min, S. Chong, G. R. Holtom, and X. S. Xie, "Label-free imaging of heme proteins with two-photon excited photothermal lens microscopy," *Appl. Phys. Lett.* **96**(11), 113701 (2010).

1. Introduction

A series of nonlinear optical techniques, such as two-photon excitation fluorescence (TPEF) [1–3], second-harmonic generation (SHG) [4,5], third-harmonic generation (THG) [6,7], coherent anti-Stokes Raman scattering (CARS) [8,9], stimulated parametric emission (SPE) [10], nonresonant four-wave mixing (NFWM) [11], two-photon absorption (TPA) [12] and stimulated Raman scattering (SRS) [13–15], has been developed in the field of high spatial resolution microscopy, opening up a wide range of applications in physics, chemistry, and biology. Nonlinear optical microscopy (NLOM) offers several advantages over linear optical microscopy. The nonlinear dependence of the signal intensity on the intensity of the tightly focused excitation light provides inherent optical sectioning capability and reduction of detrimental out-of-focus interactions such as photoinduced damage and photobleaching [1–14]. TPEF microscopy is typically used to image specific molecular species in samples that

have been labeled by fluorophores [1–3]. Other nonlinear microscopies can image unlabeled samples. SHG microscopy [4,5] has been used to image oriented and organized structures. THG [6,7] and NFWM [11] microscopies can produce images based on refractive index variations. CARS [8,9] and SRS [13–15] microscopies, which employ two-color fields, provide image contrast derived from vibrations of the chemical components or the thermodynamic state of the sample. SPE [10] and TPA [12] microscopies, which utilize two-photon electronic resonance, allow the imaging of absorbing molecules. CARS and SPE signals contain a high nonresonant FWM background, while TPA and SRS microscopies theoretically do not have a nonresonant background. In practice, however, such a background may be generated in TPA and SRS microscopies by other nonlinear optical processes including cross-phase modulation. The loss or gain in TPA [16] and SRS [13] induced by two-color excitation pulses needs to be discriminated from the laser $1/f$ noise. The $1/f$ noise can be reduced by modulating the intensity of one of the two-color pulses at a high frequency and measuring the modulation transfer to the other pulse.

NLOM also has the advantage of being able to image deeper within samples than linear optical microscopy when near-IR excitation is employed that falls in the window for maximum optical transparency in biological systems [2,17,18]. Nonetheless, deep imaging is intrinsically difficult since the excitation light is attenuated by scattering and absorption in the sample. Consequently, the signal intensity in the focal region decreases exponentially with increasing penetration depth. The signal intensity in the focal region can be maintained by compensating the reduced excitation intensity at the focus by increasing the excitation power at the sample surface. However, this increases the background signal, which includes nonlinear signals generated in out-of-focus regions. At high excitation intensities, the background signal becomes comparable to the signal intensity in the focal region. Thus, the large out-of-focus signals limit the achievable imaging depth [19]. Several techniques have been developed to suppress out-of-focus signals [20–25]. Temporal focusing suppresses out-of-focus signals in TPEF microscopy using line and plane excitation [20,21]. Adaptive optics can be used to reject the background by differential aberration imaging [22] and to recover diffraction-limited performance by compensating for wavefront distortion [23] in TPEF microscopy. Structured illumination microscopy (non-superresolution) in which the spatial intensity is modulated by interfering two beams near the focal plane provides background rejection in wide-field one-photon excitation fluorescence (OPEF) imaging [24]. Focal modulation microscopy (FMM), which generates interference at the focal point by modulating the relative phase between two beams in confocal OPEF microscopy, not only results in background rejection, but it also enhances the resolution [25].

NLOM overcomes the diffraction-limited spatial resolution due to the nonlinearity of the imaging process [6]. However, NLOM using near-IR light has a lower spatial resolution than linear optical microscopy employing visible light because the effective focal spot size depends more on the wavelength than the intensity. The spatial resolution of linear optical microscopy has been improved by various techniques [26–32], whereas the spatial resolution in NLOM has been enhanced only by stimulated emission depletion TPEF [33], 4π confocal TPEF [34] and CARS using annular phase masks [35].

Here, we present a spatial overlap modulation (SPOM) technique that can overcome the limits of conventional NLOMs. SPOM nonlinear optical microscopy (SPOM-NOM) enhances the three-dimensional (3D) spatial resolution and suppresses out-of-focus signals in all NLOMs, and provides the detection of the loss or gain by TPA and SRS. SPOM-NOM is similar to FMM. However, NLOM combined with FMM has not yet been demonstrated experimentally. We demonstrate that the SPOM technique can be combined with all NLOMs by employing spatial nonlinear intensity modulation through SPOM of two-color pulses.

2. Principle of spatial overlap modulation nonlinear optical microscopy

In SPOM-NOM, we use nonlinear optical processes that are excited by a combination of two-color pulses. Such processes include nondegenerate TPEF, TPA, sum-frequency generation (SFG), FWM, SPE, CARS, and SRS. The spatial overlap between the two-color pulses is

temporally modulated by beam pointing modulation as shown in Fig. 1(a). As an example, we use nondegenerate TPEF microscopy to illustrate the principle of this technique. As shown in Fig. 1(b), the focal position of the excitation pulse at ω_1 is temporally modulated with displacement, δ_0 , at a modulation frequency, f , whereas that of the other excitation pulse at ω_2 is fixed. We consider the TPEF intensity modulation at positions $-\delta_0$, 0 , and $+\delta_0$. Because the TPEF intensity at $\omega_1 + \omega_2$ is proportional to the product of the intensities of the excitation pulses, the TPEF intensity, $I_{\text{TPEF}}(r, t)$, is temporally modulated according to $I_{\text{TPEF}}(r, t) \propto I_1(r - \delta_0 \cos 2\pi ft, z)I_2(r)$. The TPEF intensity at $r = 0$ is modulated at a frequency of $2f$, while those at $-\delta_0$ and $+\delta_0$ are modulated at a frequency of f as shown in Fig. 1(c). Thus, the frequency dependence of the TPEF signal varies from the center to the edge of the irradiated region. Assuming Gaussian beam profiles, the distortion of beam profiles from purely sinusoidal waves appears as high harmonic components. From the even-multiple frequency components of the modulation frequency, we can acquire information from a smaller volume than the interaction volume. Therefore, the spatial resolution is enhanced by sensing the even-multiple frequency components of the modulation frequency. However, modulation in a straight line in the lateral (x) direction does not improve the spatial resolution in the y direction. This problem can be solved by moving the focal position of one pulse in a spiral locus in the xy plane as expressed by $I_1(x - \delta_0 \cos 2\pi ft \cos 2\pi f_0 t, y - \delta_0 \cos 2\pi ft \sin 2\pi f_0 t, z)$. This spiral modulation enhances the 3D spatial resolution. We refer to these techniques as straight and spiral SPOM-NOM. Moreover, since the modulation depth of the spatial overlap in the focal region is much greater than those in out-of-focus regions, out-of-focus background signals, which limit the obtainable imaging depth, are well suppressed. Thus, SPOM-NOM can be used to extend the achievable imaging depth.

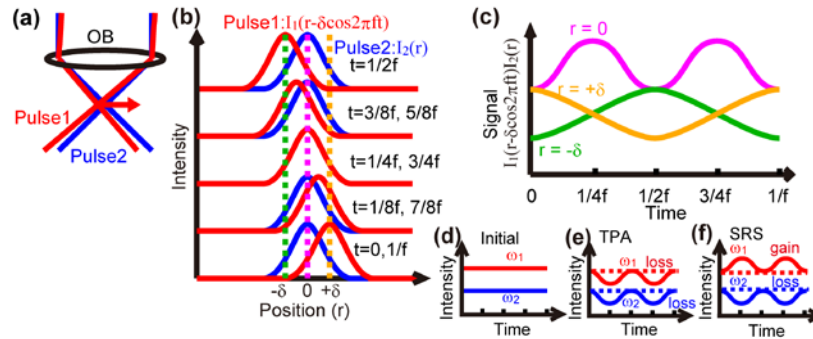


Fig. 1. Modulation scheme and principle of SPOM-NOM. (a) Beam-pointing modulation. The spatial overlap between the two-color pulses is modulated by moving the focal position of one of the two pulses by beam pointing modulation. (b) Transition of the intensity distributions of the two pulses in SPOM. The focal position of one pulse is moved with simple harmonic motion between $-\delta$ and $+\delta$ at a frequency of f . (c) Variation of the nondegenerate TPEF intensity by SPOM. The TPEF intensity at position 0 is modulated at a frequency of $2f$, while those at positions $-\delta$ and $+\delta$ are modulated at a frequency of f . By exploiting the different frequency dependences, information in a volume smaller than the interaction volume can be obtained from the demodulation signal at $2f$. (d) Input intensities for TPA or SRS detection. (e) Intensity changes by TPA. (f) Intensity changes by SRS.

By using SPOM at a modulation frequency of f without intensity modulation of the excitation pulses (Fig. 1(d)), the laser intensities are modulated at a frequency of $2f$ with the loss or gain from TPA (Fig. 1(e)) and SRS (Fig. 1(f)). Thus, SPOM enables the loss or gain from TPA and SRS to be detected through a lock-in amplifier with a demodulation frequency of $2mf$ ($m = 1, 2, 3, \dots$).

We define the relation between signals in conventional nonlinear microscopy and SPOM-NOM. As an example, we consider nondegenerate TPEF signals. In conventional

nondegenerate TPEF microscopy using two-color pulses at instantaneous intensities of $I_1(r,z,t)$ and $I_2(r,z,t)$, the TPEF signal is expressed by

$$\begin{aligned} S_{\text{conv}}(r, z) &= \eta \sigma^{(2)} \int_0^T I_1(r, z, t) I_2(r, z, t) dt \\ &\approx \eta \sigma^{(2)} I_1^{(\text{peak})}(r, z) I_2^{(\text{peak})}(r, z) f_L \tau T \\ &\approx \frac{\eta \sigma^{(2)}}{f_L \tau} I_1^{(\text{ave})}(r, z) I_2^{(\text{ave})}(r, z) T, \end{aligned} \quad (1)$$

where T is the pixel dwell time, $\sigma^{(2)}$ is the two-photon absorption cross section, τ is the pulse duration, f_L is the pulse repetition rate, $I^{(\text{peak})}$ is the peak intensity, and $I^{(\text{ave})}$ is the time-averaged intensity. η is the proportionality coefficient including the detection efficiency, the fluorescence quantum efficiency, and so on. r and z are radial and axial coordinates, respectively, which denote the distances from the focal point. Since the SPOM-NOM signal for beam pointing modulation is detected through a lock-in amplifier with a demodulation frequency of $2mf$ ($m = 1, 2, 3, \dots$), the demodulated TPEF signal in SPOM-NOM can be written as

$$\begin{aligned} S_{2mf}(r, z) &\approx \frac{\eta \sigma^{(2)} I_2^{(\text{ave})}(r, z)}{f_L \tau} \\ &\times \int_0^T I_1^{(\text{ave})}(r - \delta(z) \cos 2\pi ft, z) \cos(2\pi 2mft + m\pi) dt, \end{aligned} \quad (2)$$

where f is the modulation frequency. In the beam-pointing modulation, $\delta(z)$ is expressed by

$$\delta(z) = \frac{\delta_0(z + f_{\text{OB}})}{f_{\text{OB}}}, \quad (3)$$

where δ_0 is the maximum displacement of the focal spot and f_{OB} is the focal length of the objective lens. When $m = \delta_0 = 0$, Eq. (2) corresponds to Eq. (1) and expresses the number of total collected photons during SPOM-NOM at each point. According to Eq. (2), the demodulated signal in SPOM-NOM can be negative. To estimate the difference between the number of required photons per pixel in SPOM-NOM and that in conventional TPEF microscopy for the same signal intensity and acquisition time, we simplify Eq. (2) by making a few approximations. By employing a Taylor expansion, I_1 can be written as

$$\begin{aligned} I_1^{(\text{ave})}(r - \delta(z) \cos 2\pi ft) &= \sum_{l=0}^{\infty} \frac{1}{l!} \left. \frac{\partial^l I_1^{(\text{ave})}(r, z)}{\partial r^l} \right|_{r=0} (r - \delta(z) \cos 2\pi ft)^l \\ &= \sum_{l=0}^{\infty} \frac{1}{l!} \left. \frac{\partial^l I_1^{(\text{ave})}(r, z)}{\partial r^l} \right|_{r=0} \\ &\times \sum_{k=0}^l \frac{l!}{k!(l-k)!} r^{l-k} \{-\delta(z)\}^k \cos^k 2\pi ft. \end{aligned} \quad (4)$$

Since $\delta(z)$ is much smaller and T is much longer than $1/2mf$, I_1 components that cannot be neglected in the integration in Eq. (2) are expressed by

$$\begin{aligned}
& \sum_{l=2m}^{\infty} \frac{1}{l!} \left. \frac{\partial^l I_1^{(\text{ave})}(r, z)}{\partial r^l} \right|_{r=0} \frac{l!}{(2m)!(l-2m)!} r^{l-2m} \{-\delta(z)\}^{2m} \frac{\cos 2\pi 2mft}{2^{2m-1}} \\
&= \sum_{l=2m}^{\infty} \frac{1}{(l-2m)!} \left. \frac{\partial^{l-2m}}{\partial r^{l-2m}} \left(\frac{\partial^{2m} I_1^{(\text{ave})}(r, z)}{\partial r^{2m}} \right) \right|_{r=0} r^{l-2m} \\
&\times \frac{1}{2^{2m-1} (2m)!} \delta(z)^{2m} \cos 2\pi 2mft \\
&= \frac{\partial^{2m} I_1^{(\text{ave})}(r)}{\partial r^{2m}} \frac{1}{2^{2m-1} (2m)!} \delta(z)^{2m} \cos 2\pi 2mft.
\end{aligned} \tag{5}$$

Using Eqs. (2) and (5), the demodulated TPEF intensity in SPOM-NOM can be approximated by

$$S_{2mf}(r, z) \approx (-1)^m \frac{\eta \sigma^{(2)} I_2^{(\text{ave})}(r, z) \delta(z)^{2m} \frac{\partial^{2m} I_1^{(\text{ave})}(r)}{\partial r^{2m}} T}{2^{2m} (2m)! f_L \tau}. \tag{6}$$

When the intensity profile $I_1(r, z)$ is approximated by $I_1(r, z) = I_0 w_0^2 e^{-r^2/D^2(z)} / D^2(z)$, the demodulated TPEF signal at $2f$ can be written as

$$S_{2f}(r, z) \approx \frac{\delta_0^2(z + f_{\text{OB}})^2}{2f_{\text{OB}}^2 D^2(z)} \left(1 - \frac{4r^2}{D(z)^2} \right) S_{\text{conv}}(r, z), \tag{7}$$

where

$$D(z) = w_0 \sqrt{1 + z^2 / \rho^2} \tag{8}$$

and

$$\rho = \frac{n\pi w_0^2}{\lambda_c}. \tag{9}$$

Here, w_0 is the focal spot radius ($1/e^2$), λ_c is the central wavelength, and n is the refractive index. Equation (7) indicates that the spatial resolution of SPOM-NOM at $2f$ is enhanced by a factor of $\delta_0^2(z + f_{\text{OB}})^2 (1 - 4r^2 / D(z)^2) / (2f_{\text{OB}}^2 D^2(z))$ relative to that of conventional TPEF microscopy.

According to Eq. (7), the demodulated signal in SPOM is proportional to the square of the maximum displacement of the focal spot and is inversely proportional to the square of the focal spot size. Thus, when the focal spot size is spread by wavefront distortion at large depths, the demodulated signal in the focal region is reduced compared with those in out-of-focus regions near the sample surface. Consequently, the signal-to-background ratio is reduced. However, the reduced demodulated signal can be compensated by increasing the maximum displacement of the focal spot. Then, the out-of-focus background from the sample surface is hardly increased. Therefore, the signal-to-background ratio can be enhanced even when the focal spot size is spread by wavefront distortion. Of course, the wavefront distortion can be compensated by adaptive optics [23].

The maximum magnitudes of $\partial^2 I_1 / \partial r^2$, $\partial^4 I_1 / \partial r^4$, $\partial^6 I_1 / \partial r^6$, and $\partial^8 I_1 / \partial r^8$ can be written as $4I_1^1 / w_0^2$, $48I_1^1 / w_0^4$, $960I_1^1 / w_0^6$, and $2304I_1^1 / w_0^8$, respectively. Thus, the demodulated TPEF intensities in SPOM-NOM at demodulation frequencies of $2f$, $4f$, $6f$, and $8f$ are respectively reduced by factors of $\delta_0^2 / 2w_0^2$, $\delta_0^4 / 8w_0^4$, $\delta_0^6 / 48w_0^6$, and $\delta_0^8 / 384w_0^8$ compared with the conventional TPEF intensity. If δ_0 is set to $w_0/2$, the number of the required photons per pixel in SPOM-NOM at a demodulation frequency of $2f$ is eight times greater than that in

conventional TPEF microscopy to obtain the same signal. Under this condition, we can achieve a sufficiently high enhancement of the spatial resolution. If the numbers of total corrected photons per pixel are equal both in microscopies, the demodulated TPEF intensity in SPOM-NOM at $2f$ will be eight times lower than the TPEF intensity in conventional microscopy.

3. Experimental

3.1. Experimental setup

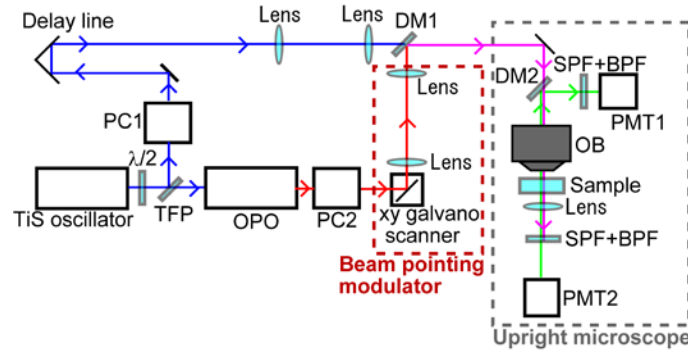


Fig. 2. SPOM-NOM setup. OPO: optical parametric oscillator, PCs: pre-chirpers, DMs: dichroic mirrors, OB: objective lens, SPF: short-pass filter, BPF: band-pass filter, PMT: photomultiplier tube.

The experimental setup is illustrated in Fig. 2. We used a custom-built nonlinear microscope with a mode-locked Ti:sapphire oscillator (Coherent, Mira-900F) and an optical parametric oscillator (OPO; Coherent, Mira-OPO-IR-FAN) operating at a repetition rate of 76 MHz. To compensate for dispersion of all the optical components before the focal point of the microscope objective (OB), the pulses were passed through an S-BSM81 prism pair and a chirp mirror pair at 60 bounces (PC1) for the Ti:sapphire oscillator and an S-TIH6 prism pair (PC2) for the OPO. The two-color pulses from the oscillators were overlapped in time using an optical delay line and in space by a dichroic mirror (DM1). The pulses were focused into the samples by an oil-immersion objective lens (Olympus, UPLSAPO100 × O, NA 1.4) for high-resolution imaging or a water immersion objective lens (Olympus, LUMFLN 60 × W, NA: 1.1) for deep imaging. We used oil-immersion and water-immersion objective lenses under the underfilling back aperture condition for which the fill factors for both beams were almost 80% ($1/e^2$) and 65% ($1/e^2$), respectively. At the focal point, the pulse durations of the Ti:sapphire and OPO pulses were almost 90 and 80 fs, respectively. The spatial overlap between the two-color pulses was modulated by beam pointing modulation of the OPO pulse using a two-axis galvano scanner (Cambridge Technology, 6210H). The two-color pulses were modulated at $f = 1$ kHz for straight SPOM-NOM and $f = 0.2$ kHz and $f_0 = 1$ kHz for spiral SPOM-NOM. The modulation frequency f was limited by the frequency response of the galvano-scanner. Nonlinear signals were detected by photomultiplier tubes (PMT1 for TPEF and PMT2 for SFG, CARS, and SRS) (Hamamatsu Photonics, H7422A-40) through a lock-in amplifier (Stanford Research Systems, SR830). Because of the low modulation frequency, the lock-in amplifier also had a low demodulation frequency. Thus, we had to increase the exposure time per pixel. As a result, an exposure time of 30 ms/pixel was used, except for 3D deep imaging of brain tissues in yellow fluorescent protein (YFP)-expressing mice (for which an exposure time of 20 ms/pixel was used). In TPEF and SFG imaging, to exclude the excitation wavelengths, short-pass filters (Semrock, FF01-720/SP-25) were placed in front of both PMT1 and PMT2. Band-pass filters (Semrock, FF01-520/35-25 for TPEF from fluorescent beads; Semrock, FF01-542/27-25 for TPEF from brain tissues in YFP-expressing mice; Semrock, FF01-435/40-25 for SFG or Semrock, FF01-628/40-25 for CARS; Semrock, FF01-780/12-25 for SRS) were also placed in front of the PMTs to select the detection

wavelength. The sample was scanned by a three-axis piezoelectric transducer stage (Piezosystem Jena, Tritor 101 CAP). Since the laser powers at the focal point in deep TPEF imaging decay as $\exp(-az)$ due to absorption and scattering, the laser powers and the PMT gain were increased by $\exp(az)$ and $\exp(2az)$ to maintain a constant TPEF intensity at the focal point, respectively. A Ti:sapphire input power at the sample of 1 mW was used for high-resolution TPEF and SFG imaging and SRS imaging and 80 mW was used for deep TPEF imaging. The OPO input powers at the sample were 1 mW for high-resolution TPEF and SFG imaging, 80 mW for deep TPEF imaging, and 6 mW for SRS imaging.

3.2. Sample preparation

In order to characterize the spatial resolution, we prepared a 100-nm fluorescent polystyrene bead as a point object. Yellow-green (505/515) fluorescent polystyrene beads (Molecular Probes) with a diameter of 100 nm were coated on a glass slide, index matched with an immersion oil (Olympus, IMMOIL-F30CC) and covered with a cover glass. We also employed yellow-green (505/515) fluorescent polystyrene beads (Molecular Probes) with a diameter of 200 nm coated on a glass slide with a high density. To demonstrate the improved spatial resolution of label-free NLOM, we also prepared samples for SFG imaging. We pounded granulated sugar in a mortar and used it in SFG imaging. We also employed a quartz crystal cut on 90° to investigate the axial response of SFG imaging. SFG appear only at interfaces, while in the bulk medium the sum-frequency waves destructively interfere due to the Gouy phase shift [36].

To demonstrate the background suppression by SPOM-NOM, we prepared a solution of cyan-fluorescent protein with a concentration of 10 mg/cc in HEPES NaOH buffer (50 mM, pH 7.4), which was set in a glass container with an optical path length of 70 μm . We also made a tissue-like phantom as a highly scattering sample. We added 45 μL of a 2- μm fluorescent polystyrene bead solution (Molecular Probes) with a concentration of 4.55×10^9 beads/mL to 160 μL of low-melting-point agarose gel, pipetted it onto a 35-mm Petri dish with a cover glass bottom and covered it with another cover glass. The phantom contained 2- μm fluorescent polystyrene beads at a concentration of 1.0×10^9 beads/mL as scatterers and tracers. This concentration corresponds to scattering coefficients of 115 and 99.3 cm^{-1} for 775 and 1000 nm, respectively.

In our biological application, we used a brain of a transgenic mouse line, the 1-YFP line H (YFP-H) [37]. In the brain of YFP-H mouse, yellow fluorescent protein (YFP) is expressed in a subpopulation of neurons; the expression is localized in most pyramidal neurons in the hippocampus and neurons with somata in layers V and VI in the cerebral cortex. An adult YFP-H male mouse (eight weeks old) was deeply anesthetized with pentobarbital (Somnopenyl) and transcardially perfused with 4% PFA/PBS. The whole brains were removed and subjected to post-fixation in 4% PFA/PBS at 4 $^\circ\text{C}$ for 8 h. To fairly compare the deep imaging capability of the conventional technique with that of SPOM technique, the fixed brain tissue was left at 4 $^\circ\text{C}$ for six weeks; this was sufficiently long that the scattering coefficient remained constant during long measurements by the two techniques. Thus, the scattering coefficient was almost three times higher than that typically measured immediately after the brain is extracted from a mouse and is post-fixed. The two-photon excitation cross section for YFP at a combination of 800 and 1100 nm was the same as the two-photon excitation cross section at 926 nm because there is no intermediate resonant level [38].

3.3. Enhancement of the spatial resolution

We experimentally characterized the spatial resolution of SPOM-NOM at a demodulation frequency of $2f$ by employing 775 and 1000-nm pulses with a maximum focus displacement of 100 nm. Figures 3(a) and 3(b) respectively show TPEF images in the xz plane of a 100-nm fluorescent bead obtained by conventional microscopy (775-nm pulse only) and SPOM-NOM (775 and 1000-nm pulses). We obtained lateral (x) full width at half maximums (FWHMs) of 0.31 ± 0.034 μm and 0.19 ± 0.021 μm for conventional microscopy and SPOM-NOM, respectively as illustrated in Fig. 3(c). These FWHMs were obtained by taking the average of

five measurements. The lateral FWHM has been improved by a factor of 1.6. The negative lateral response of SPOM-NOM was also observed. When nonlinear media lie next to each other, a destructive superposition of negative and positive responses provides an enhancement in spatial resolution. Thus, the effective spatial resolution is enhanced not only by the narrower FWHM, but also by the negative response because of destructive superposition of negative and positive responses. The negative values after destructive superposition can be replaced with 0 because negative values indicate side lobes. In terms of the Rayleigh criterion, two, equally bright, object points can just be resolved when the maximum of the intensity distribution of one coincides with the first minimum of the other. Although, the signal drop rate at the center of the two object points depends on the shape of the distribution, there is a drop of approximately 30%. Instead of the Rayleigh criterion, we superimposed the measured TPEF intensity profile of a 100-nm fluorescent bead and the TPEF intensity profile obtained by shifting it, and evaluated the shifting distance where the signal drop rate at the center of the two fluorescent beads was 30%. Thus, we obtained the resolved distance of 0.38 μm and 0.25 μm for conventional microscopy and SPOM-NOM, respectively as shown in Fig. 3(d). The axial (z) FWHMs of conventional microscopy and SPOM-NOM are $0.76 \pm 0.039 \mu\text{m}$ and $0.55 \pm 0.031 \mu\text{m}$, respectively (Fig. 3(e)). These results clearly demonstrate that SPOM-NOM has a greater spatial resolution than conventional TPEF microscopy. However, modulation in a

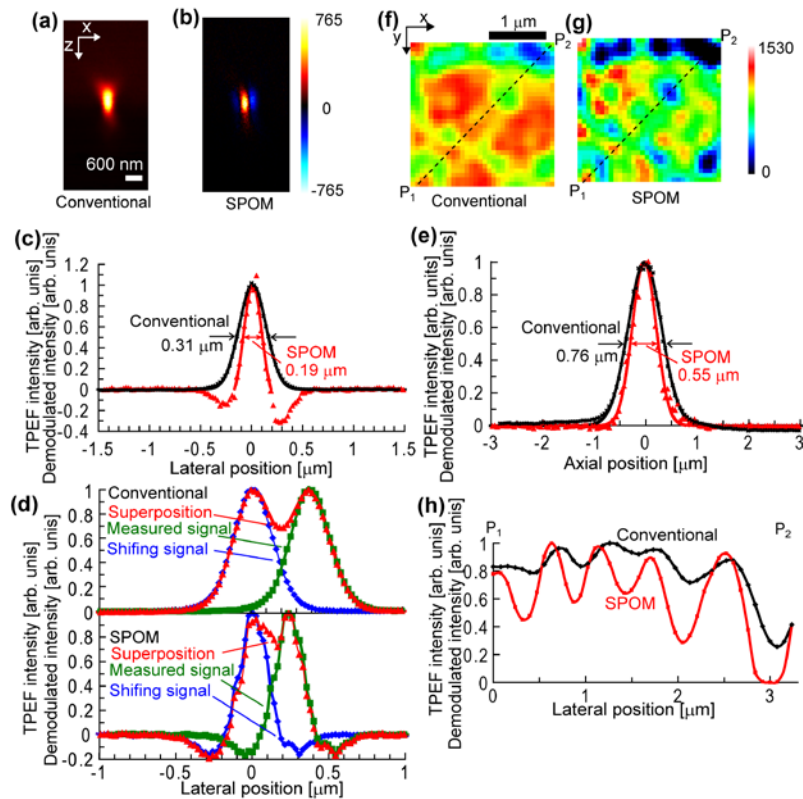


Fig. 3. Enhancement of the spatial resolution in TPEF imaging by SPOM-NOM. (a, b) TPEF images of a 100-nm fluorescent bead by (a) conventional microscopy and (b) SPOM-NOM. (c) TPEF intensity and demodulated intensity profiles in the x direction in images (a) and (b), which corresponds to the lateral response. (d) Superposition of the measured TPEF intensity profile of a 100-nm fluorescent bead and the TPEF intensity profile obtained by shifting it. (e) TPEF intensity and demodulated intensity profiles in the z direction in images (a) and (b), which corresponds to the axial response. (f, g) TPEF images of 200-nm fluorescent beads obtained by (f) conventional microscopy and (g) SPOM-NOM. The sharper response of SPOM-NOM results in a better spatial separation of the beads. (h) Intensity and demodulated intensity profiles along the dashed lines in (f) and (g).

straight line in the lateral (x) direction did not improve the spatial resolution in the y direction. This problem could be solved by spiral SPOM-NOM. The spiral modulation enhanced the 3D spatial resolution. Figures 3(f) and 3(g) show TPEF images in the xy plane of 200-nm fluorescent beads. As shown in Fig. 3(h), the enhanced 3D spatial resolution results in better spatial separation of the beads.

To further demonstrate the improved spatial resolution of label-free NLOM, we acquired SFG images in the xz plane of pounded sugar using 775 and 1000-nm pulses. Figures 4(a) and 4(b) show SFG images obtained by conventional microscopy and SPOM-NOM, respectively. The profiles along the dashed lines in the SFG images demonstrate that the sharper response of SPOM-NOM gives rise to a well-resolved image as illustrated in Fig. 4(c). We also measured the modulation displacement dependence of the one-dimensional SFG intensity distribution in the axial direction near the surface of a quartz crystal. As shown in Fig. 4(d), the FWHMs of the axial intensity distribution of SFG by conventional microscopy and SPOM-NOM with a maximum displacement of the focus of 400, 300, 200, and 100 nm are 1.52 ± 0.062 , 0.90 ± 0.055 , 0.87 ± 0.059 , 0.85 ± 0.065 , and 0.82 ± 0.085 μm , respectively. Because the SFG signal was integrated over the xy plane, these FWHMs are broader than those of TPEF from 100-nm fluorescent beads (see Fig. 3(d)). We also plotted the demodulated intensity as a function of the maximum displacement of the focus in Fig. 4(e). The demodulated intensity is proportional to the 1.9th power of the maximum displacement of the focus. We can confirm that the maximum displacement of about half the focal spot radius provides an axial resolution that is 1.8 times greater than that of conventional SFG microscopy. We also obtained axial responses with FWHMs of 1.22 ± 0.056 and 1.78 ± 0.068 μm for SHG using 775 and 1000-nm pulses, respectively. As illustrated in Fig. 4(d), the axial resolution of SPOM-NOM was also improved; in this case, it was improved by 1.5 times compared with that of conventional SHG microscopy at 775 nm.

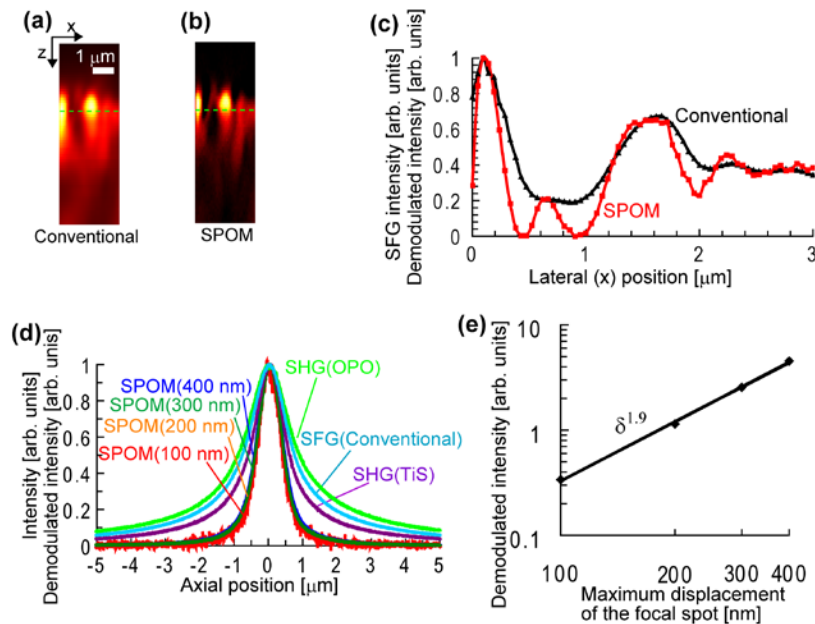


Fig. 4. Enhancement of the spatial resolution in SFG imaging by SPOM-NOM. (a, b) SFG images of granulated sugar pounded in a mortar obtained by (a) conventional microscopy and (b) SPOM-NOM. (c) Intensity and demodulated intensity profiles along the dashed lines in (a) and (b). (d) Line profiles of (demodulated) SFG and SHG intensities in the axial direction near the surface of a quartz crystal cut on 90° . (e) The maximum displacement dependence of the demodulated intensity.

3.4. Suppression of out-of-focus signals for deep imaging

As an important application of SPOM-NOM, we investigated the suppression of out-of-focus signals. Figure 5(a) shows TPEF signal distributions in the axial direction near the interface between a cyan-fluorescent protein (CFP) solution and a glass slide obtained by straight SPOM-NOM employing 775 and 1000-nm pulses with a maximum displacement of the focus of 400 nm. At axial positions below 20 μm , the focal point was located in the CFP solution. We obtained the out-of-focus TPEF signals of 3.85×10^{-3} and 3.79×10^{-5} for conventional TPEF microscopy and SPOMNOM, respectively, by taking the averages of TPEF intensities at axial positions from 40 μm to 80 μm . The out-of-focus TPEF signals were suppressed by a factor of 102. Figure 5(b) illustrates the axial position dependence of SFG signals generated near the surface of a quartz crystal using the straight SPOM technique with 775 and 1000-nm pulses. We obtained the out-of-focus SFG signals of 3.44×10^{-3} and 3.43×10^{-5} for conventional SFG microscopy and SPOMNOM, respectively, by taking the averages of SFG intensities at axial positions from $-40 \mu\text{m}$ to $-20 \mu\text{m}$. The out-of-focus SFG signals were suppressed by a factor of 100. Thus, we could suppress the out-of-focus TPEF and SFG signals.

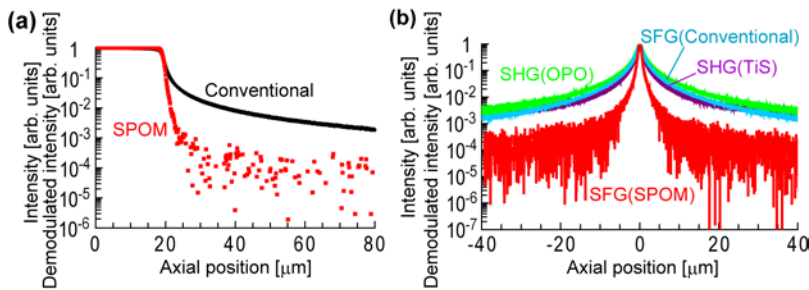


Fig. 5. Suppression of out-of-focus nonlinear signals by the SPOM technique. (a) Line profiles of TPEF intensity and demodulated TPEF intensity in the axial direction near the interface between a cyan-fluorescent protein solution and a glass slide. (b) Intensity distributions of SFG with 775 and 1000-nm pulses, SHG with 775-nm pulses and SHG with 1000-nm pulses, and demodulated SFG distribution along the axial direction near the surface of a quartz crystal cut on 90° .

We used spiral SPOM-NOM with 775 and 1000-nm pulses to image fluorescently labeled beads in the tissue-like phantom. The observed images, which were normalized at each penetration depth, are depicted in Fig. 6(a). The compensation coefficients α for the losses of the laser powers at the focal point due to scattering were set to 115 cm^{-1} and 99 cm^{-1} for 775 and 1000 nm, respectively. Compared with images obtained by the conventional technique (1000-nm pulse only), we found that the background signals were dramatically suppressed by the SPOM technique. Thus, the obtainable imaging depth could be extended by the SPOM technique. To quantify the background suppression, the contrast ratio between the TPEF intensity of the beads in the focal plane and the background TPEF intensity are plotted as a function of penetration depth in Fig. 6(b). We obtained the signal and background intensities by taking the averages of TPEF intensities at 9-neighboring pixels (3×3 pixels) around the center of bead, and at 25-neighboring pixels (5×5 pixels) around the dark pixel in each image, respectively. This demonstrates that SPOM-NOM increases the contrast ratio by more than 20 times.

We also demonstrate deep imaging of fixed mouse brain tissue expressing an YFP in a subpopulation of neurons. Figures 7(a) and 7(b) show 3D TPEF images, which were reconstructed from 295 xy ($15 \times 30 \mu\text{m}^2$, 32×64 pixels) images obtained at depth increments of 1 μm by conventional microscopy and y -direction straight SPOM-NOM with 800 and 1100-nm pulses, respectively. Figures 7(c) and 7(d) show maximum-intensity side projections of the image stacks obtained by the conventional and SPOM techniques. The compensation coefficient α for the losses of the laser powers at the focal point due to scattering was set to

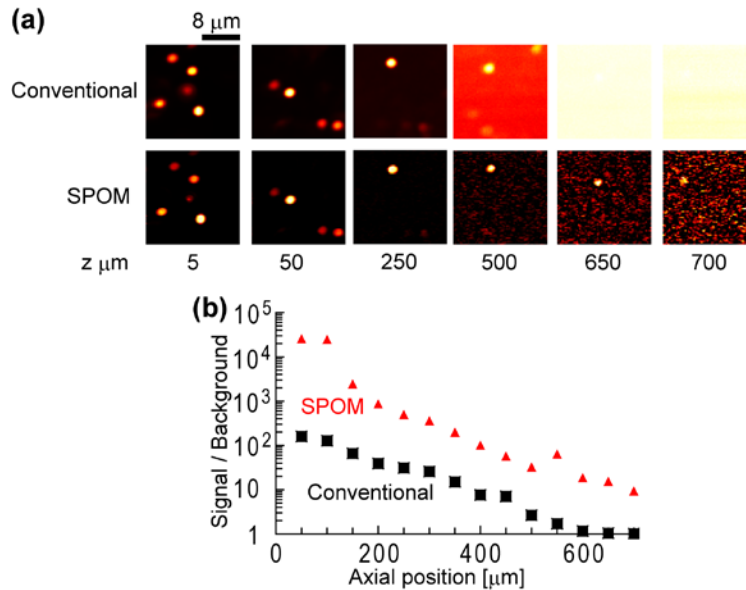


Fig. 6. (a) TPEF images of a tissue-like phantom, composed of low-melting-point agarose gel containing 2- μm fluorescent polystyrene beads at a concentration of 1.0×10^9 beads/mL, by conventional microscopy (upper panel) and SPOM-NOM (bottom panel). The background that includes the out-of-focus TPEF signals has been suppressed by the SPOM technique. (b) The contrast ratio between the TPEF intensity of fluorescent beads in the focal plane and the background TPEF intensity as a function of penetration depth in a tissue-like phantom.

170 cm^{-1} , which was obtained from the decay curve of fluorescence signals given by conventional TPEF microscopy with 800 and 1100-nm pulses before deep imaging. This coefficient is almost three times higher than those which have been reported [16,17]. This is because to avoid undesirable changes in the scattering coefficient during measurements by both techniques, the fixed brain tissue was left for six weeks. The background fluorescence in deep regions (layers II or III) by the conventional technique was higher than those reported for the conventional technique [16,17] due to the high scattering coefficient. We found that the dendrites were clearly visible in the TPEF image obtained by the SPOM technique and that there was no background TPEF signals at large depths where TPEF signals at the focal spot by the conventional technique were swamped by the background TPEF signals. These results indicate that the SPOM technique enhances the spatial resolution and suppresses out-of-focus signals in deep regions. Thus, we realized background-free deep imaging by the SPOM technique.

3.5. Sensing the SRS loss without the intensity modulation transfer technique

We applied the SPOM technique to detect the loss due to SRS. By using the straight SPOM technique, we obtained SRS images of 1- μm polystyrene beads at frequency differences of 3051 cm^{-1} (775 and 1015-nm pulses) and 3333 cm^{-1} (775 and 1045-nm pulses), as shown in Figs. 8(a) and 8(b). Because a signal-to-noise ratio (SNR) was low due to the low modulation frequency, we increased the maximum focus displacement up to 600 nm. The frequency difference of 3051 cm^{-1} is assigned to aromatic C–H stretching vibrations, whereas the frequency difference of 3333 cm^{-1} is nonresonant. Under the same conditions as those for SRS imaging, we also obtained CARS images using the conventional technique, as shown in Figs. 8(c) and 8(d). The nonresonant signals in the SRS images are well suppressed, whereas those in the CARS image are relatively large. The advantage of SRS imaging (i.e., suppression of nonresonant signals) was realized by the SPOM technique. However, we could not enhance the spatial resolution because of the large maximum focus displacement.

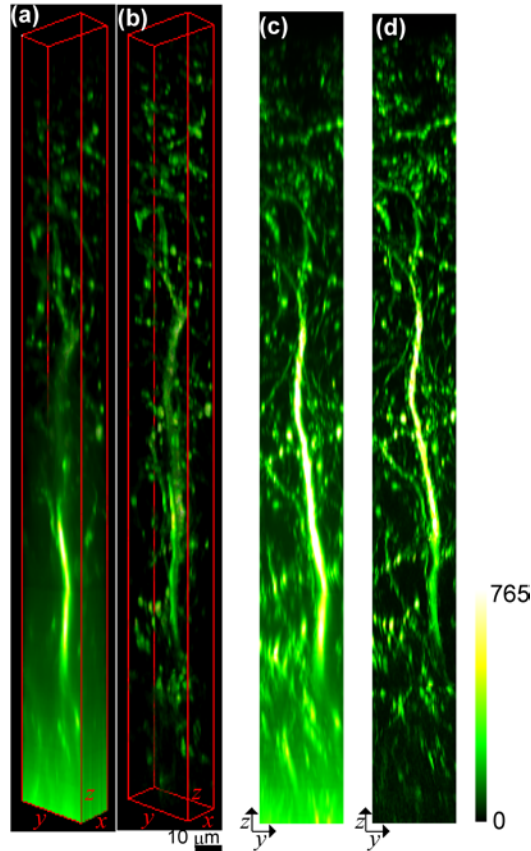


Fig. 7. TPEF images of fixed mouse brain tissues, which express a YFP in a subset of neurons. (a, b) 3D TPEF images obtained by (a) conventional microscopy and (b) SPOM-NOM. Each 3D image was reconstructed from 295 xy images (32×64 pixels) obtained at depth increments of $1 \mu\text{m}$. (c, d) Maximum-intensity x projections of the image stacks for (c) conventional microscopy and (d) SPOM-NOM in (a) and (b).

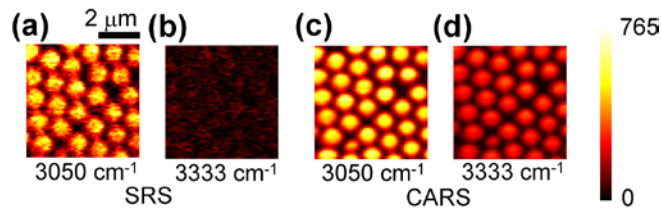


Fig. 8. Sensing loss by SRS with the SPOM technique. (a, b) SRS images at frequency differences of (a) 3051 cm^{-1} (aromatic C–H stretching vibration) and (b) 3333 cm^{-1} (nonresonant) by SPOM-NOM. (c, d) CARS images at frequency differences of (c) 3051 cm^{-1} and (d) 3333 cm^{-1} by conventional microscopy. The nonresonant signals in the SRS image are suppressed, whereas those in the CARS image are relatively large.

4. Discussion and conclusions

Using SPOM-NOM, we have demonstrated that the 3D spatial resolution can be enhanced by a factor of 1.4–1.8, out-of-focus signals can be suppressed by a factor of 100, and loss imaging by SRS without intensity modulation can be achieved. Because nonlinear signals are sensitive to the excitation intensity variations due to the nonlinearity, tightly focused beams can realize optical sectioning in NLOM. In contrast, the enhanced imaging performances in

SPOM-NOM are obtained by additional nonlinearity caused by spatially modulating the product of the excitation intensities. In these demonstrations, the modulation frequency of SPOM was limited to 1 kHz by the frequency response of the galvano-scanner employed. Because the laser 1/f noise was large due to the low modulation frequency, deep TPEF and SRS imaging has a smaller SNR than shot-noise-limited detection. Because of the low modulation frequency, the pixel dwell time was 1000 times longer than typical TPEF microscopy. Here, we discuss a method to implement SPOM-NOM at normal scanning speeds and at high SNRs. The demodulated intensity per pixel in SPOM-NOM at $2f$ with a maximum displacement of about half the focal spot radius, which gives a sufficiently high resolution enhancement, is eight times lower than the TPEF intensity in conventional microscopy under the same conditions (i.e., pixel dwell time, laser powers, and total collected photons). However, SPOM-NOM suppresses noises such as the laser 1/f noise, the thermal noise, and the quantization noise. By increasing the modulation and demodulation frequencies, the laser 1/f noise, which is often the largest noise in deep TPEF and SRS imaging, could be suppressed. In addition, under the extreme condition that the out-of-focus background is much larger than the signal near the focal region, the effective dynamic range of the detection system in conventional microscopy is narrowed by the background compared with that in SPOM-NOM. Thus, quantization noise occurs in conventional microscopy, whereas it can be suppressed in SPOM-NOM. The thermal noise can be suppressed by cooling the detection system. Thus, SPOM-NOM can realize shot-noise-limited detection. Therefore, although the TPEF signal in SPOM-NOM is lower than that in conventional microscopy, the SNR of SPOM-NOM with the shot-noise-limited detection can be higher than that of conventional TPEF microscopy. The dwell time in SPOM-NOM can be improved to the order of microseconds by shot-noise-limited detection using a high-speed pointing modulator such as an electro-optic deflector. Nevertheless, there are two problems in deep imaging. Attenuation of the beam within the absorbing and scattering sample changes the focus position [19], which may create artifacts in deep imaging. The other problem is the signal reduction and artifacts by wavefront distortion that occurs at large depths. These problems could be solved by using adaptive optics to compensate wavefront distortion and the shift of the focus position. Thus, the imaging performance can be improved further by combining SPOM-NOM with adaptive optics. SPOM-NOM with shot-noise-limited detection would open up super-resolution imaging at large depths, which has been demonstrated only by fluorescence imaging [39].

Because the intensities of incident two-color pulses are not temporally modulated in SPOM-NOM, the intensity changes of the two-color pulses induced by TPA and SRS can be simultaneously detected by two detectors, which cannot be realized by intensity modulation transfer. If the incident two-color pulses have equal intensities, the magnitudes of the intensity changes of the two-color pulses by TPA and SRS will also be equal. However, SRS leads to the loss of the pump light (ω_2) and the amplification (gain) of Stokes light (ω_1), while TPA results in the losses of the two-color pulses (ω_1 and ω_2). By subtracting the intensity change of the pump light (ω_2) from that of the Stokes light (ω_1), the SRS signal is doubled, whereas the TPA signal is removed. In contrast, by adding the intensity changes of the two-color pulse, the TPA signal is doubled, while the SRS signal is removed. Thus, the SPOM technique enables us to separate SRS signals from TPA signals, which may be the background in SRS microscopy using intensity modulation transfer. Although Kerr lensing or thermal lensing artifacts appearing in TPA and SRS imaging [40] may not be ignored, the SPOM-NOM could make simultaneous TPA and SRS imaging possible.

Finally, it should be noted that this SPOM technique can be installed on all NLOMs just by implementing modulation of the beam pointing, as demonstrated by some of the experiments in the present study. The two-color pulses required in SPOM-NOM can be also generated by dividing a single pulse with a broadband spectrum into two spectral bands. Thus, conventional NLOM can be easily converted to SPOM-NOM. The SPOM technique cannot only exploit the full potential of NLOMs, but it can also extend their capabilities.

Acknowledgments

We thank Prof. Kazuyoshi Itoh and Prof. Yasuyuki Ozeki of Osaka University for providing OPO (Coherent, Mira-OPO-IR-S1) for initial testing. We also thank Dr. Hiroshi Hama, and Mr. Hiroshi Kurokawa from RIKEN for providing the YFP-H mouse. This work was partially supported by Sumitomo Foundation and Konica Minolta Science and Technology Foundation.